Article

Molecular mechanism for isoform-selective inhibition of acyl protein thioesterases 1 and 2 (APT1 and APT2)

Sang Joon Won, Dahvid Davda, Kristin J. Labby, Sin Ye Hwang, Rachel E. Pricer, Jaimeen D. Majmudar, Kira A Armacost, Laura A Rodriguez, Christina L Rodriguez, Fei San Chong, Kristopher A. Torossian, Jasmine Palakurthi, Edward S. Hur, Jennifer L. Meagher, Charles L. Brooks, Jeanne A. Stuckey, and Brent R. Martin

ACS Chem. Biol., **Just Accepted Manuscript** • DOI: 10.1021/acschembio.6b00720 • Publication Date (Web): 17 Oct 2016

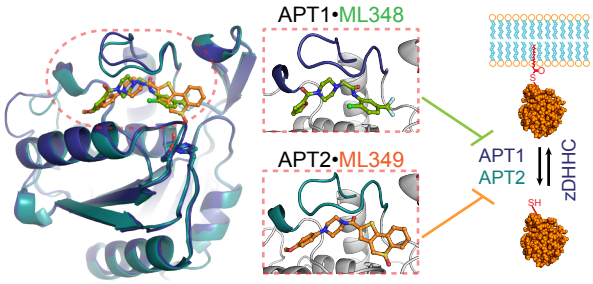
APT1•ML348
APT2•ML349
APT1
APT2
zDHHC

Molecular mechanism for isoform-selective inhibition of acyl protein thioesterases 1 and 2 (APT1 and APT2)

Sang Joon Won[1], Dahvid Davda[1, 2], Kristin J. Labby[2], Sin Ye Hwang[2], Rachel Pricer[1,4], Jaimeen D. Majmudar[2], Kira A. Armacost[2,3], Laura A. Rodriguez[2], Christina L. Rodriguez[2], Fei San Chong[2], Kristopher A. Torossian[2], Jasmine Palakurthi[2], Edward S. Hur[2], Jennifer L. Meagher[4], Charles L. Brooks III[1, 2,3], Jeanne A. Stuckey[4], and Brent R. Martin[1,2,*]

[1]Program in Chemical Biology, [2]Department of Chemistry, [3]Department of Biophysics, and [4]Life Sciences Institute, University of Michigan, 930 N. University Ave., Ann Arbor, MI 48109, USA

*To whom correspondence should be addressed: brentrm@umich.edu

Abstract

Post-translational *S*-palmitoylation directs the trafficking and membrane localization of hundreds of cellular proteins, often involving a coordinated palmitoylation cycle that requires both protein acyl transferases (PATs) and acyl protein thioesterases (APTs) to actively re-distribute *S*-palmitoylated proteins towards different cellular membrane compartments. This process is necessary for the trafficking and oncogenic signaling of *S*-palmitoylated Ras isoforms, and potentially many peripheral membrane proteins. The de-palmitoylating enzymes APT1 and APT2 are separately conserved in all vertebrates, suggesting unique functional roles for each enzyme. The recent discovery of the APT isoform-selective inhibitors ML348 and ML349 has opened new possibilities to probe the function of each enzyme, yet it remains unclear how each inhibitor achieves orthogonal inhibition. Herein we report the high-resolution structure of human APT2 in complex with ML349 (1.64 Å), as well as the complementary structure of human APT1 bound to ML348 (1.55 Å). Although the overall peptide backbone structures are nearly identical, each inhibitor adopts a distinct conformation within each active site. In APT1, ML348 is positioned above the catalytic triad, but in APT2, the sulfonyl group of ML349 forms hydrogen bonds with active site resident waters to indirectly engage the catalytic triad and oxyanion hole. Reciprocal mutagenesis and activity profiling revealed several differing residues surrounding the active site that serve as critical gatekeepers for isoform accessibility and dynamics. Structural and biochemical analysis suggests the inhibitors occupy a putative acyl-binding region, establishing the mechanism for isoform-specific inhibition, hydrolysis of acyl substrates, and structural orthogonality important for future probe development.

Introduction

Post-translational *S*-palmitoylation anchors target proteins to membranes using a high-energy thioester, which can be readily hydrolyzed by enzymes or other cellular nucleophiles. In contrast, stable modifications like *N*-myristoylation and *S*-prenylation modify proteins via an amide or thioether linkage. Thus, while some proteins evolved as targets of stable lipidation, others use reversible membrane anchors for dynamic spatial regulation. Indeed, blocking Ras palmitoylation attenuates growth signaling and transformation in mutant cells[1]. Similarly, G proteins are rapidly de-palmitoylated following activation[2], potentially redistributing active signaling proteins to attenuate signaling. While such rapid de-palmitoylation events may be enzyme-mediated, signal-dependent conformational changes could still be necessary to expose the *S*-palmitoylated cysteine to promote enzymatic hydrolysis.

The first characterized cytosolic protein de-palmitoylase, acyl protein thioesterase (APT1/LYPLA1), was identified biochemically from rat liver[3]. Although it was previously annotated as a lysophospholipase[4], both rat and yeast APT1 exhibit >65-fold to >2000-fold greater catalytic efficiencies (k_{cat}/K_m) as a $G_s\alpha$ protein de-palmitoylase[5, 6], respectively. Rat and yeast APT1 were each shown to catalyze the de-palmitoylation of $G_i\alpha_1$ (*N*-myristoylated and *S*-palmitoylated) 10-fold to 70-fold faster than Ras (*S*-farnesylated and *S*-palmitoylated)[6], respectively, demonstrating the enzyme can discriminate between different *S*-palmitoylated substrates. Nevertheless, thioester hydrolysis is significantly more exergonic than ester hydrolysis, which likely accounts for the majority of rate acceleration. APT2 (LYPLA2) shares 68% protein sequence identity with APT1[7], and displays similar Ras de-palmitoylase and lysophospholipase activity *in vitro*[7, 8]. While APT1 and APT2 likely share many common substrates, in cellular assays only APT2 affects the palmitoylation of GAP-43[9], while only APT1 participates in the de-palmitoylation of BK potassium channels[10] and the melanoma adhesion molecule (MCAM)[11]. However, these observed isoform-specific activities could also represent differential over-expression, knockdown, or subcellular localization in each model. Overall, many

studies of protein de-palmitoylation rely on the dual APT1/APT2 inhibitor Palmostatin B[12], which obscures the contributions from each individual enzyme. Nonetheless, dual APT1/APT2 inhibition disrupts over-expressed Ras trafficking and reverts certain malignant phenotypes[12].

Later screening efforts identified piperazine amide competitive inhibitors with exquisite selectivity for APT1 and APT2[13-15] (**Figure 1a)**. The APT1 inhibitor ML348 and the APT2 inhibitor ML349 are isoform-selective, relatively potent (K_i = 200-300 nM), and exhibit orthogonality beyond the solubility of each probe[15]. Because both inhibitors incorporate a common piperazine amide linked to a 5-membered heterocycle (thiophene or furan), each was hypothesized to occupy a similar position in the active-site[16]. Since there is no reported structure of APT2, the structural elements that impart inhibitor orthogonality and substrate selectivity have remained elusive. Here we present the co-crystal structures of APT1 and APT2 binding to their respective selective inhibitors. Surprisingly, neither inhibitor directly hydrogen bonds to amino acid side chains, but rather coordinate structural waters and occlude access to the catalytic residues. Mutagenesis along the β5-α2 loop and the G3 helix revealed the basis for inhibitor selectivity, which involves several residues that influence distinct loop conformations between APT1 and APT2. These elements engage each inhibitor, forming a hydrophobic fatty acyl-binding channel adjacent to the catalytic triad. Overall, these findings provide mechanistic insight to isoform-selective substrate specificity and reveal new directions for inhibitor optimization.

Results

Co-crystal structures of APT1·ML348 and APT2·ML349. Differential scanning fluorimetry indicates a ~5 °C higher melting temperature (T_m) in APT1 (59.2 °C) relative to APT2 (54.4 °C) (**Figure 1b**). Thus, crystallization could be disfavored by additional disorder in APT2. Upon ligand binding, both APT1 and APT2 are stabilized by 3.5 - 3.7 °C. Similar values were measured using a thermal shift assay, where heat denaturation and centrifugation are used to

monitor protein solubility[17] (**Figure 1c**). Again, APT1 is more thermally stable than APT2 by 4 °C, and inhibitor engagement considerably impedes denaturation.

Using this information, we readily obtained co-crystals of both APT1·ML348 and APT2·ML349. The structure of APT2 has not been reported, and therefore obtaining this model was critical for understanding the origins of inhibitor selectivity. Atomic structures of APT1·ML348 and APT2·ML349 were subsequently determined at 1.55 Å and 1.64 Å resolution, respectively (**Table 1**). Although a previously reported APT1 structure implied formation of a weak dimer[18], both APT1·ML348 and APT2·ML349 form distinct dimer interfaces in each respective asymmetric unit, suggesting that oligomerization is likely an artifact of crystallization.

Each APT structure adopts an atypical α/β hydrolase fold featuring a central, seven-stranded, mostly parallel β-sheet, corresponding to strands β1-β3 and β6-β9, surrounded by variable lengths of loops, helices and strands (**Figures 2a-b**). In both enzymes, the nucleophilic serine (APT1-Ser199/APT2-Ser122) assumes the typical strained conformation at the apex of the elbow between β6-α3, whereas the histidine base (APT1-His209/APT2-His210) and aspartate (APT1-Asp174/APT2-Asp176) are positioned on nearby extended loops between β9-α5 and β8-α4, respectively. APT1 and APT2 include non-canonical insertions of an anti-parallel β4-β5 sheet, the corresponding β5-α2 loop, and a short G1 helix. Furthermore, both enzymes replace the fourth α-helix of the canonical fold with a short helical segment, termed G3, which is structurally divergent between the APT1·ML348 and APT2·ML349 structures, and an additional short helix in APT2, termed G4.

Unlike other α/β hydrolase lipases, APT homologues lack a distinctive ‘cap’ domain important for substrate binding and a flexible ‘lid’ that protects the active site from solvent. Instead, APTs may use the β5-α2 loop, which is flanked on one side by G1/β8-α4 loop and G3 helix on the other to form a relatively long (~20 Å) putative acyl-binding channel wherein both ML348 and ML349 reside. This hydrophobic channel shows varying degrees of openness between APT1, APT1·ML348 and APT2·ML349 (**Figures 2c-d and S1**). In the distant bacterial

homologue FTT258 (PDB: 4F21), the analogous loop domain demonstrates dynamic conformational changes proposed to define the active and inactive states, suggesting the loop closes upon substrate binding to initiate hydrolysis[19]. However, this substrate driven conformational change could differ among APTs, especially because the shorter G1 helix and the non-canonical β4-β5 sheet replace this loop in all vertebrate APTs (**Figures S2a-b**). Although part of β4 and G1 pack with the β5-α2 loop to form one end of the channel, the overall functional role of the β4-β5 sheet and G1 motif remains speculative. The resulting hydrophobic channel has sufficient space and polarity to accommodate long chain fatty acyl chains. Because APT enzymes are more active towards long chain fatty acyl substrates[20], shorter acyl chains may not provide enough free energy to counteract the entopic penalty of binding (increasing K_m) or bind too deep in the channel. Either would impede substrate orientation and activity. In comparison to the unbound structure, ML348 binding pushes out the β5-α2 loop, suggesting loop flexibility in this non-canonical region likely contributes to inhibitor engagement.

Structural features of ML348 and ML349 engagement. In the structure of APT1·ML348, two waters form hydrogen bonds to the anilide carbonyl, whereas in APT2 the same waters interact with the piperazine amide carbonyl (**Figures 3a-d)**. Clearly, the piperazine amide carbonyls of ML348 and ML349 motifs interact differently in each enzyme, showing no clear structure-activity relationship shared between APT1 and APT2[13-15]. Regardless, the bulk of both ML348 and ML349 molecules occupy the hydrophobic channel where their water-coordinated carbonyl groups are superimposed. One of these waters forms a hydrogen bond to the backbone carbonyl of APT1-Gln83/APT2-Pro86 and the backbone amide of APT1-Gly77/APT2-Met79, whereas the second forms hydrogen bonds to APT1-Glu84/ APT2-Glu87. In addition, APT1-Trp145/APT2-Trp-148 forms putative π-π stacking interactions with the aromatic anilide of ML348 and the thiophene of ML349, respectively. On the other end, APT1-Phe181/APT2-

Phe183 also forms a π-π stacking interaction between the ML348 furanyl group and ML349 anisole group, respectively.

The G3 helix has weak sequence similarity between APT1 and APT2, suggesting it may be a site of functional divergence **(Figures S2a-b)**. In APT1, Arg149 of G3 forms a hydrogen bond with a water molecule that coordinates the ML348 piperazinyl amide carbonyl and the Pro80 backbone carbonyl in the β5-α2 loop (**Figure S3a**). In contrast, His152 in the APT2 G3 helix forms a π-π stacking with the ML349 anisole group, and Arg153 forms a hydrogen bond with Asp84 side chain of the β5-α2 loop (**Figure S3b**). Most importantly, both the anilide ring of ML348 and the thiochromene heterocycle of ML349 are positioned directly above the catalytic triad, blocking substrate access. The ML348 trifluoromethyl substituent passively blocks the catalytic triad through a series of hydrophobic contacts, including those with Leu30, Leu176, and the hinge residue Ile75. In contrast, the ML349 sulfone group participates in a hydrogen bond network with water molecules, making indirect contacts with both the oxyanion hole and the catalytic triad (**Figures 3a-d**).

At first glance, we initially hypothesized the ML349 sulfone might act as a tetrahedral transition state inhibitor since the sulfonyl group of ML349 is in proximity to the catalytic residues Ser122, His210, and the oxyanion hole backbone carbonyl oxygens of Gln123 and Leu33 (**Figures 3b and 3d**). On closer analysis, ML349 appears to form indirect hydrogen bonds to APT2 via two intervening water molecules, each tethered by hydrogen bonds to the catalytic machinery in the active site. One water molecule forms a hydrogen bond to an oxyanion hole amide through its oxygen lone pair, while also serving as a hydrogen bond donor to an ML349 sulfone oxygen. The other water molecule is positioned near the histidine base (His210) where it would normally become polarized to participate in acyl-intermediate hydrolysis, but instead forms a hydrogen bond to the other ML349 sulfone oxygen.

Next, we examined if the enzyme-inhibitor complex depends on the presence of the sulfonyl oxygens. A racemic ML349-sulfoxide derivative demonstrated some residual inhibition, but

ML349-thioether completely lost any ability to bind APT2 (**Figures 4b and S4a-c**). In order to test whether the serine nucleophile participates in ML349 binding, we synthesized an ML349-fluorescein (ML349-FL) conjugate to probe active site binding by fluorescence polarization, independent of substrate hydrolysis (**Figure 4a**). Interestingly, both ML349 and the ML349-FL bind the catalytic dead APT2-S122A mutant with similar affinity (**Figures 4a-b**), confirming Ser122 does not engage the thiochomene sulfone. Pre-treatment with either ML349 or hexadecylfluorophosphonate (HDFP) blocked ML349-FL polarization with APT2, ruling out any alternative binding mechanisms while confirming overlap between HDFP and ML349 binding sites. Furthermore, both activity-based and fluorescence polarization competition studies confirmed that ML349 has at least 20-fold lower K_d than the racemic ML349-sulfoxide towards APT2, and no significant binding by ML349-thioether (**Figure 4b and S4a**).

Molecular Dynamics Simulations. To complement the characterization noted above, we carried out molecular dynamics simulations of the enzyme-ligand complexes to investigate how each sulfonyl oxygen of ML349 interacts in the presence of active site resident waters to stabilize the enzyme-inhibitor complex in comparison with sulfoxide variants. In order to monitor enzyme-inhibitor interactions, we constructed the distance between two designated atoms throughout the course of the simulated trajectories. These distances were displayed graphically over 50 ns periods from separate simulations for ML349 and the two *in silico* generated enantiomers (*S)*-ML349 sulfoxide (oxygen atom pointing towards His210) and (*R)*-ML349 sulfoxide (oxygen pointing towards oxyanion hole) **(Figure 4c)**. Whereas, the sulfonyl containing ML349 showed essentially no motion in the active site during our simulations, both (*S)*-ML349-sulfoxide and (*R*)-ML349-sulfoxide – enzyme simulations displayed increased fluctuations at His210 (**Figures 4d-f**). The (*R*)-ML349-sulfoxide showed significantly more fluctuation than the (*S)*-ML349-sulfoxide, suggesting the pro-(*S*) sulfone oxygen may play a more significant role in active site stabilization. All together, these simulations demonstrate how both sulfone oxygens

of ML349 minimize disorder in the active site by indirectly engaging the catalytic residues through water-mediated hydrogen bonds, and are consistent with the findings from the thermal denaturation and kinetic analysis.

The β5-α2 loop and G3 helix are responsible for inhibitor selectivity. APT1 and APT2 have only a few divergent residues in the ligand-binding region (**Figure 5a**). In order to examine whether these positions are responsible for functional discrimination between ML348 and ML349, we performed reciprocal site-directed mutagenesis between APT1 and APT2 at these sites and carried out steady-state kinetic assays with the fluorogenic substrate resorufin acetate (ResOAc)[15] (**Figures 5b and S5a-d**). As confirmation of proper fold, essentially every reciprocal mutant displayed similar K_m values except for APT1-L176M, which might be explained by its position close to the catalytic triad (**Figures S2b and S5a**). APT1-Ile75 (Leu78 in APT2) introduces a steric clash with the trifluoromethyl group of ML348 (**Figure 5c**), and may disrupt ML349 binding. Indeed, the APT1-I75L variant reduced ML348 binding by almost 10-fold (K_i = 2.2 μM), concurrent with enhanced sensitivity to ML349 (K_i = 370 nM). The analogous APT2-L78I mutant only partially mirrored the reversal observed in APT1-I75L, yielding measurable ML348 binding (K_i = 5.8 μM), but introduces a new steric clash at the ML349 thiophene sulfur to weaken ML349 binding. Thus, Ile75 and Leu78 play important roles in dictating selectivity, but these roles are distinct with each inhibitor.

Since the reciprocal mutations at APT1-I75L/APT2-L78I do not fully reconstitute the observed potency and orthogonality of the wild type enzymes, synergistic residues were profiled by combining several reciprocal mutations. The triple APT1-I75L/S82A/Q83P mutant completely abolished ML348 inhibition, but showed weaker ML349 potency (K_i = 1.2 μM) compared to just the single I75L mutant (K_i = 370 nM). Since the APT1-Q83P mutation alone had no effect on selectivity, we examined if APT1-S82 cooperates with APT1-I75 to impart inhibitor orthogonality. Interestingly, the double mutant APT1-I75L/S82A slightly improved ML348 and ML349 inhibition

compared to APT1-I75L alone. The triple mutant APT1-I75L/S82A/Q83P no longer binds ML348, and loses significant potency for ML349. Taken together, this data demonstrate that the selectivity effect cannot be isolated to a single mutation, and S82A synergizes with Q83P to impact ML348 selectivity. Alternatively, the single APT2-P86Q and the double mutant APT2-L78I/A85S have essentially the same K_i values as either wild-type APT2 or APT2-L78I. Since the APT2 triple mutant L78I/A85S/P86Q improved ML348 potency, neither A85S nor P86Q by itself has much effect on preventing ML348 binding. As shown for APT1, the synergetic effect is observed when both residues are mutated together. Ultimately, switching the G3 helix between APT1 and APT2 led to the most robust selectivity reversal, where APT1-I75L/S82A/Q83P/R149H/A150R/S151A was potently inhibited by ML349 (K_i = 180 nM) and lost all potency for ML348. The reciprocal mutant APT2-L78I/A85S/P86Q/H152R/R153A/A154S was similarly inhibited by ML348 (K_i = 430 nM) had no residual inhibition by ML349. Clearly, the G3 helix influences β5-α2 loop dynamics to differentially engage ML348 and ML349, through interactions with the ML348 piperazinyl amide and the ML349 methoxyphenyl ring. Altogether, these structural features form the basis for orthogonal inhibition through a combination of differential flexibility and steric constraints.

Substrates and selective inhibitors engage a common acyl-binding pocket. Based on the arrangement of hydrophobic residues, we predict the acyl chain of native substrates lies in the same channel as ML348 and ML349. Interestingly, HDFP increased the T_m of each APT enzyme by over 10 °C (**Figure S6)**, suggesting lipid engagement provides a major source of energetic stabilization that decreases the K_d for long chain acyl substrates. To explore acyl engagement more directly, we performed product competition studies with ML349-FL. While oleic acid is competitive with ML349-FL binding, the observed IC_{50} value (9.9 ± 0.6 μM) is above the 6 μM critical micelle concentration (CMC) for the lipid (**Figure S7**)[21]. Incubation with 1-oleoyl-2-hydroxy-*sn*-glycero-3-phosphocholine produced slightly more potent ML349-FL

competition (IC_{50} = 4.3 ± 0.4 μM), although it also serves as a substrate and releases oleic acid. Interestingly, the catalytic dead APT2-S122A mutant showed no ML349-FL competition with 1-oleoyl-2-hydroxy-*sn*-glycero-3-phosphocholine. Thus, any competition is likely driven by released oleic acid upon lysophosphatidylcholine hydrolysis, and subject to the same potential micellar affects. To overcome this experimental obstacle, we directly assayed acyl binding using the environmentally sensitive acyl-fluorophore BODIPY-FL-C_{16}, which exhibits increased fluorescence in nonpolar environments[22]. A constant, sub-micellar concentration of BODIPY-FL-C_{16} was incubated with increasing concentrations of each enzyme, reporting dose-dependent, saturable fluorescence enhancement with APT1 (K_d = 2.5 ± 0.5 μM) and APT2 (K_d = 2.8 ± 0.5 μM) (**Figure 6a**). Furthermore, BODIPY-FL-C_{16} exhibited a dose-dependent reduction in fluorescence after addition of ML348 in APT1 or ML349 in APT2, further supporting competition for the enclosed acyl-binding pocket (**Figures 6b-c**). Although the precise BODIPY-FL-C_{16} orientation and binding mode are unknown, this assay confirms BODIPY engagement to a non-polar site displaced selectively in each APT isoform by its corresponding competitive inhibitor.

Discussion

APT1 and APT2 are broadly invoked whenever describing the dynamic turnover of *S*-palmitoylation on proteins[16]. While ML348 and ML349 superficially share a common piperazinyl amide chemotype, our high-resolution structural analyses reveal distinct binding modes that block access to the catalytic triad and occlude the putative acyl-binding pocket. Ligand engagement by a hydrophobic channel is not surprising, since APT1 and APT2 react exceptionally fast with aliphatic fluorophosphonate probes and HDFP, and much slower with polar, PEG-fluorophosphonate probes[15, 23]. The potent dual APT1/APT2 inhibitor Palmostatin B also incorporates a 10-carbon chain [12], reinforcing the benefit conferred by an acyl binding element.

Based on structural and sequence alignment of APTs across vertebrates, any determinants promoting functional orthogonality between APT1 and APT2 are not immediately obvious (**Figure S2b**). Several studies suggest that APT1 and APT2 harbor intrinsic substrate preferences[9, 10], and clearly APT1 and APT2 possess sufficient structural variance to enable isoform-selective inhibition. Herein we carried out reciprocal mutagenesis at divergent residues distal from the catalytic triad, revealing functional differences affecting inhibitor engagement. Although definitive evidence supporting the precise mode of acyl group engagement will require further crystallographic analysis, our current biochemical competition data demonstrates that each isoform-selective inhibitor occludes acyl engagement across the non-polar channel, which likely forms upon substrate engagement by the closure of the β5-α2 loop. Alternatively, the acyl group could potentially occupy the shallow groove contiguous along the catalytic site and acyl-binding pocket (**Figure S8**). Since this groove is largely solvent exposed with mixed polarity, it more likely helps dock lysophospholipid head groups or the palmitoylated protein domains. While this model is intuitive, any functional role for the adjacent groove will require further biochemical studies, potentially after HDFP inactivation. However, part of the β8/α4 region also features several divergent residues closer to the active site. These additional residues could cooperate in substrate acquisition, supporting additional investigation to dissect further functional divergence. Overall, the observed inhibitor orthogonality is solely derived from the acyl-binding channel, thus any substrate selectivity beyond acyl-chain selection is more likely promoted through distal sites not engaged by either ML348 or ML349.

Based the structural models presented, we speculate APT enzymes primary hydrolyze substrates with reduced membrane partitioning, including lysophospholipids, prostaglandin esters, or singly *S*-palmitoylated substrates. Further *S*-acylation of each APT enzyme likely localizes the enzyme in close proximity to membrane-bound substrates, thereby enhancing substrate acquisition and relative activity. Following substrate recruitment and acyl engagement, we propose that the β5-α2 loop closes to encapsulate the non-polar acyl chain, providing

significant enzyme stabilization to drive polar coordination of the acyl thioester. Additional interactions may further align the peptide, culminating in the thioester hydrolysis and subsequent release of product. This model readily accommodates *S*-palmitoylated sites near the protein termini or disordered regions, allowing the peptide and acyl chain to thread along the contiguous groove. Dually lipidated proteins, such as *N*-myristoylated and *S*-palmitoylated Lck and $G_i\alpha_1$, may require additional rearrangements to engage the active site. Here the *N*-myristoyl group could expand the binding pocket by shifting the flexible β5-α2 loop to accommodate both lipids, or one acyl group could remain engaged in the membrane and thread next to the β4-β5 sheets and G1 helix. Deciphering the precise mechanism of substrate engagement will likely require additional structural analysis, potentially capturing native substrates with a catalytic dead enzyme, or through the design of tailored fluorophosphonate probes to mimic acylated peptide substrates.

Overall, the structures of APT1·ML348 and APT2·ML349 show highly similar active sites with distinct inhibitor conformations despite a related chemotype. Inhibitor selectivity depends on distinct residues lining a divergent flexible loop, reminiscent of the lid domain of related bacterial hydrolases[19]. More potent inhibitors may be optimized to directly engage each protein, potentially by displacing active site waters, or through extended engagement of the shallow proximal groove. Furthermore, we report the unique sulfonyl-engagement of ML349 by APT2, suggesting further exploration of sulfonyl functional groups when optimizing active site-directed reversible hydrolase inhibitors. Ultimately, this structural analysis highlights the subtle differences between APT1 and APT2 leveraged by ML348 and ML349, which will provide value in future studies profiling the physiological function and substrates of each enzyme across both lipidated peptides and metabolites.

Methods

See Supporting Information for additional methods.

Protein expression, purification, and crystallization. APT1 and APT2 genes were amplified from human 239T cell cDNA and inserted into pMCSG7 to introduce an in-frame N-terminal poly-histidine tag for expression. BL21 (DE3) *E.coli* (Novagen) cultures (OD_{600} = 0.6) were induced with 0.5 mM IPTG for 16 h at 25 ºC. Cell pellets were resuspended in 50 mM HEPES pH 7.8, 300 mM NaCl, 10% glycerol, sonicated, and centrifuged at 35,000x g for 30 min. Talon cobalt affinity beads (Clontech) were incubated with the cleared supernatant for 1 h, and then washed with 50 mM HEPES pH 7.8, 150 mM NaCl, and 1 mM imidazole buffer. The proteins were eluted with 50 mM HEPES, 150 mM NaCl, 150 mM imidazole buffer. The eluted samples were dialyzed overnight in the presence of TEV protease to remove excess imidazole and to cleave the HisTag, yielding ~10 mg / mL of protein. Protein samples were supplemented with 20% glycerol and stored at -80 ºC. For crystallization, protein stock solutions pre-incubated with inhibitors were prepared at 8 mg / mL and supplemented with 5 mM dithiothreitol (DTT). APT1 was incubated with 3 mM ML348 and APT2 was incubated with 1 mM ML349 for at least one hour at 4 °C before setting crystal trays for incubation at 20 °C. Crystals were produced by sitting drop vapor diffusion with drops containing 2 µL of enzyme-inhibitor complex and 2 µL of reservoir solution. For APT1·ML348, the best-diffracting crystals were formed from reservoir solution containing 0.1 M sodium citrate pH 5.5, 22-24% PEG 3350, and 200 mM $MgCl_2$. For APT2·ML349, the best-diffracting crystals were formed from reservoir solution containing 0.1 mM sodium citrate pH 5.5, 20-24% PEG 3350. Larger, better diffracting crystals were formed by microseeding 1 d after setup. After 1-2 weeks, thin plate crystals formed. Reservoir solution was supplemented with 25% ethylene glycol for cryopreservation.

Data Collection and Structure Determination. Diffraction data for APT1·ML348 and APT2·ML349 were collected on the Advanced Photon Source LS-CAT beamlines 21-ID-D and 21-ID-G, respectively. The data were processed with MOSFLM[24] and scaled with SCALA[25]. APT1·ML348 was solved to 1.55 Å resolution by molecular replacement using MOLREP[26] with

the A chain of APT1 (PDB ID: 1FJ2) as the search model. The structure of APT2·ML349 was solved to 1.64 Å resolution by molecular replacement via Balbes[27], which also used the APT1 structure as the search model. Both structures went through iterative rounds of manual electron density fitting and structural refinement in Coot[28] and Buster[29]. Difference electron density maps contoured at 2σ showed the presence an inhibitor associated with each protein chain. Coordinates and restraint files for each ligand were created by Grade[29] with the mogul+qm option. Data collection and refinement statistics for each structure are listed in **Table 1**. Figures were generated using PyMol Molecular Graphics system (Schrödinger). Atomic coordinates for APT1·ML348 and APT2·ML349 have been deposited in the PDB as entries 5SYM and 5SYN, respectively.

Molecular Dynamics Simulations. Molecular dynamics simulations were performed for APT2·ML349, APT2·ML349 (*R*-sulfoxide), and APT2·ML349 (*S*-sulfoxide) using the CHARMM macromolecular modeling program[30], version c39b2, as described in the Supporting Information.

Supporting Information

Methods including thermal denaturation, molecular dynamics simulations, fluorescence binding assays, synthetic procedures and characterization, and additional figures as described in the text.

Author Contributions. K.J.L., R.P., and S.J.W. prepared expression plasmids. K.J.L., J.P., L.A.R., C.L.R., and S.J.W. purified proteins. F.S.C., E.S.H., J.D.M., K.A.T., and S.J.W. synthesized inhibitors. K.J.L., J.L.M., and J.P. optimized crystallization conditions. J.L.M. and J.A.S. collected X-ray data and determined structures. S.Y.H. and S.J.W. performed all inhibitor and enzyme assays. K.A.A. and C.L.B performed computational studies. S.J.W. and D.D. designed competition experiments. K.J.L., S.J.W., D.D., and B.R.M. designed other experiments.

D.D. and S.J.W. analyzed inhibition data. R.P. and S.J.W. designed figures. S.J.W., D.D., and B.R.M. wrote the paper.

Acknowledgements. We would like to thank John Tesmer (University of Michigan) for critically reading the manuscript. Financial support for these studies was provided by the National Institutes of Health R00 CA151460, DP2 GM114848, the American Heart Association 14POST20420040 (J.D.M.), and the University of Michigan.

References

[1] Willumsen, B. M., Cox, A. D., Solski, P. A., Der, C. J., and Buss, J. E. (1996) Novel determinants of H-Ras plasma membrane localization and transformation, *Oncogene 13*, 1901-1909.

[2] Wedegaertner, P. B., and Bourne, H. R. (1994) Activation and depalmitoylation of Gs[alpha], *Cell 77*, 1063-1070.

[3] Sugimoto, H., Hayashi, H., and Yamashita, S. (1996) Purification, cDNA cloning, and regulation of lysophospholipase from rat liver, *J Biol Chem 271*, 7705-7711.

[4] Yuan, B.-Z., Miller, M. J., Keck, C. L., Zimonjic, D. B., Thorgeirsson, S. S., and Popescu, N. C. (1998) Cloning, Characterization, and Chromosomal Localization of a Gene Frequently Deleted in Human Liver Cancer (DLC-1) Homologous to Rat RhoGAP, *Cancer Res 58*, 2196-2199.

[5] Duncan, J. A., and Gilman, A. G. (1998) A Cytoplasmic Acyl-Protein Thioesterase That Removes Palmitate from G Protein alpha Subunits and p21RAS, *J. Biol. Chem. 273*, 15830-15837.

[6] Duncan, J. A., and Gilman, A. G. (2002) Characterization of Saccharomyces cerevisiae Acyl-protein Thioesterase 1, the Enzyme Responsible for G Protein alpha Subunit Deacylation in Vivo, *J. Biol. Chem. 277*, 31740-31752.

[7] Toyoda, T., Sugimoto, H., and Yamashita, S. (1999) Sequence, expression in Escherichia coli, and characterization of lysophospholipase II, *Biochimica et Biophysica Acta (BBA) - Molecular and Cell Biology of Lipids 1437*, 182-193.

[8] Hedberg, C., Dekker, F. J., Rusch, M., Renner, S., Wetzel, S., Vartak, N., Gerding-Reimers, C., Bon, R. S., Bastiaens, P. I., and Waldmann, H. (2011) Development of highly potent inhibitors of the Ras-targeting human acyl protein thioesterases based on substrate similarity design, *Angew Chem Int Ed Engl 50*, 9832-9837.

[9] Tomatis, V. M., Trenchi, A., Gomez, G. A., and Daniotti, J. L. (2010) Acyl-Protein Thioesterase 2 Catalizes the Deacylation of Peripheral Membrane-Associated GAP-43, *PLoS One 5*, e15045.

[10] Tian, L., McClafferty, H., Knaus, H. G., Ruth, P., and Shipston, M. J. (2012) Distinct acyl protein transferases and thioesterases control surface expression of calcium-activated potassium channels, *J Biol Chem 287*, 14718-14725.

[11] Wang, W., Runkle, K. B., Terkowski, S. M., Ekaireb, R. I., and Witze, E. S. (2015) Protein Depalmitoylation Is Induced by Wnt5a and Promotes Polarized Cell Behavior, *J Biol Chem 290*, 15707-15716.

[12] Dekker, F. J., Rocks, O., Vartak, N., Menninger, S., Hedberg, C., Balamurugan, R., Wetzel, S., Renner, S., Gerauer, M., Scholermann, B., Rusch, M., Kramer, J. W., Rauh, D., Coates, G. W., Brunsveld, L., Bastiaens, P. I., and Waldmann, H. (2010) Small-molecule inhibition of APT1 affects Ras localization and signaling, *Nat Chem Biol 6*, 449-456.

[13] Adibekian, A., Martin, B. R., Chang, J. W., Hsu, K. L., Tsuboi, K., Bachovchin, D. A., Speers, A. E., Brown, S. J., Spicer, T., Fernandez-Vega, V., Ferguson, J., Cravatt, B. F., Hodder, P., and Rosen, H. (2010) Characterization of a Selective, Reversible Inhibitor of Lysophospholipase 2 (LYPLA2), In *Probe Reports from the NIH Molecular Libraries Program*, Bethesda (MD).

[14] Adibekian, A., Martin, B. R., Chang, J. W., Hsu, K. L., Tsuboi, K., Bachovchin, D. A., Speers, A. E., Brown, S. J., Spicer, T., Fernandez-Vega, V., Ferguson, J., Cravatt, B. F., Hodder, P., and Rosen, H. (2010) Characterization of a Selective, Reversible Inhibitor of Lysophospholipase 1 (LYPLA1), In *Probe Reports from the NIH Molecular Libraries Program*, Bethesda (MD).

[15] Adibekian, A., Martin, B. R., Chang, J. W., Hsu, K. L., Tsuboi, K., Bachovchin, D. A., Speers, A. E., Brown, S. J., Spicer, T., Fernandez-Vega, V., Ferguson, J., Hodder, P. S., Rosen, H., and Cravatt, B. F. (2012) Confirming target engagement for reversible inhibitors in vivo by kinetically tuned activity-based probes, *J Am Chem Soc 134*, 10345-10348.

[16] Davda, D., and Martin, B. R. (2014) Acyl protein thioesterase inhibitors as probes of dynamic S-palmitoylation, *MedChemComm 5*, 268-276.

[17] Molina, D. M., Jafari, R., Ignatushchenko, M., Seki, T., Larsson, E. A., Dan, C., Sreekumar, L., Cao, Y., and Nordlund, P. (2013) Monitoring Drug Target Engagement in Cells and Tissues Using the Cellular Thermal Shift Assay, *Science 341*, 84-87.

[18] Devedjiev, Y., Dauter, Z., Kuznetsov, S. R., Jones, T. L., and Derewenda, Z. S. (2000) Crystal structure of the human acyl protein thioesterase I from a single X-ray data set to 1.5 A, *Structure 8*, 1137-1146.

[19] Filippova, E. V., Weston, L. A., Kuhn, M. L., Geissler, B., Gehring, A. M., Armoush, N., Adkins, C. T., Minasov, G., Dubrovska, I., Shuvalova, L., Winsor, J. R., Lavis, L. D., Satchell, K. J., Becker, D. P., Anderson, W. F., and Johnson, R. J. (2013) Large scale structural rearrangement of a serine hydrolase from Francisella tularensis facilitates catalysis, *J Biol Chem 288*, 10522-10535.

[20] Kakugawa, S., Langton, P. F., Zebisch, M., Howell, S. A., Chang, T.-H., Liu, Y., Feizi, T., Bineva, G., O/'Reilly, N., Snijders, A. P., Jones, E. Y., and Vincent, J.-P. (2015) Notum deacylates Wnt proteins to suppress signalling activity, *Nature 519*, 187-192.

[21] Davis, B. M., Richens, J. L., and O'Shea, P. Label-Free Critical Micelle Concentration Determination of Bacterial Quorum Sensing Molecules, *Biophysical Journal 101*, 245-254.

[22] Thumser, A. E., and Storch, J. (2007) Characterization of a BODIPY-labeled {fl}uorescent fatty acid analogue. Binding to fatty acid-binding proteins, intracellular localization, and metabolism, *Molecular and Cellular Biochemistry 299*, 67-73.

[23] Martin, B. R., Wang, C., Adibekian, A., Tully, S. E., and Cravatt, B. F. (2012) Global profiling of dynamic protein palmitoylation, *Nat Methods 9*, 84-89.

[24] (1994) The CCP4 suite: programs for protein crystallography, *Acta Crystallogr D Biol Crystallogr 50*, 760-763.

[25] Evans, P. R. (2011) An introduction to data reduction: space-group determination, scaling and intensity statistics, *Acta Crystallogr D Biol Crystallogr 67*, 282-292.

[26] Vagin, A., and Teplyakov, A. (2010) Molecular replacement with MOLREP, *Acta Crystallogr D Biol Crystallogr 66*, 22-25.

[27] Long, F., Vagin, A. A., Young, P., and Murshudov, G. N. (2008) BALBES: a molecular-replacement pipeline, *Acta Crystallogr D Biol Crystallogr 64*, 125-132.

[28] Emsley, P., and Cowtan, K. (2004) Coot: model-building tools for molecular graphics, *Acta Crystallogr D Biol Crystallogr 60*, 2126-2132.

[29] Bricogne, G., Blanc, E., Brandl, M., Flensburg, C., Keller, P., Paciorek, W., Roversi, P., Shariff, A., Smart, O., Vonrhein, C., and Womack, T. (2011) BUSTER version 2.11.2, Global Phasing Ltd, Cambridge, UK.

[30] Brooks, B. R., Brooks, C. L., 3rd, Mackerell, A. D., Jr., Nilsson, L., Petrella, R. J., Roux, B., Won, Y., Archontis, G., Bartels, C., Boresch, S., Caflisch, A., Caves, L., Cui, Q., Dinner, A. R., Feig, M., Fischer, S., Gao, J., Hodoscek, M., Im, W., Kuczera, K., Lazaridis, T., Ma, J., Ovchinnikov, V., Paci, E., Pastor, R. W., Post, C. B., Pu, J. Z., Schaefer, M., Tidor, B., Venable, R. M., Woodcock, H. L., Wu, X., Yang, W., York, D. M., and Karplus,

M. (2009) CHARMM: the biomolecular simulation program, *J Comput Chem 30*, 1545-1614.

Figure Legends

Figure 1. Isoform-selective inhibitors stabilize APT1 and APT2. (*a*) Chemical structures of ML348 and ML349. (*b*) ML348 and ML349 impart dose-dependent thermal stabilization of APT1 and APT2, respectively, by differential scanning fluorimetry. (*c*) Thermal shift assay corroborates thermal stabilization of APT enzymes by selective ligands.

Figure 2. Co-crystal structures of APT1·ML348 and APT2·ML349 reveals conformational changes induced upon ligand binding. (*a*) Co-crystal structure of APT1·ML348. A 2 σ omit map is shown for ML348. The catalytic triad is indicated in sticks, and the non-canonical β4-β5 sheet, the G1 helix, and the β5-α2 loop are colored purple (*b*) Co-crystal structure of APT2·ML349. A 2 σ omit map is shown for ML349, where the catalytic triad is indicated in sticks. Other features highlighted in APT1·ML348 are colored in purple. (*c*) Structure alignment of APT1·ML348 and APT2·ML349. Regions of significant conformational differences are shown in red-dotted circles. (*d*) Structural variance of APT1 (PDB: 1FJ2) in orange and APT1·ML348 in dark blue. Significant conformation changes are observed for the G1 helix, β4-β5 stands and β5-α2 loop.

Figure 3. Distinct binding modes promote inhibitor binding in APT1 and APT2. (*a*) The hydrophobic channel of the APT1·ML348 complex from different perspectives. Side chains of residues within 3.5 Å of ML348 (green) are shown as grey sticks. Water molecules are shown as red spheres and hydrogen bonds by red dotted lines. (*b*) The hydrophobic channel of APT2·ML349 complex from different perspectives. Side chains of residues within 3.5 Å of ML349 (orange) are shown in grey sticks, with similar notation for waters and hydrogen bonds. (*c*) Two dimensional ligand plot of ML348 interactions with APT1. Red dashed lines represent hydrogen bonds and grey dashed lines indicate π-π stacking interactions. Chemical features are color coded and labeled. (*d*) Two dimensional ligand plot of ML349 with corresponding labels as described in (*c*).

Figure 4. ML349 indirectly engages the catalytic triad and oxyanion hole of APT2. (a) ML349-FL exhibits APT2-dependent fluorescence polarization. (b) Chemical structures of ML349 derivatives are shown above the dose-dependent ML349-FL displacement by ML349 derivatives in APT2 and APT2-S122A. (*c*) Structural representation of the *S* and *R* oxygen atoms comprising the ML349 sulfone group in APT2. Atomic distances are shown with dotted lines corresponding to the color schemes used to present the molecular dynamics simulations. Blue represents the distance from the His210 τ-nitrogen to ML349-*S*-oxygen. Brown represents the distance from the ML349-*S*-oxygen to Q123 backbone amide nitrogen. Red represents the distance from the ML349-*S*-oxygen to S122 oxygen. Green represents the distance from His210 τ-nitrogen to the ML349-*R*-oxygen. Black represents the distance from the ML349-*R*-oxygen to the Q123 backbone amide nitrogen. Purple represents the distance from the ML349-*R*-oxygen to the S122 oxygen. (*d*) Molecular dynamic simulation of APT2·ML349 demonstrates little active site fluctuation between the sulfone oxygens and catalytic triad. (e) Bound (*S*)-ML349-sulfoxide promotes flexibility of His210 to destabilize the active site. (f) Bound (*R*)-ML349-sulfoxide promotes flexibility even greater flexibility of His210 and similarly destabilizes the active site.

Figure 5. The divergent β5-α2 loop imparts Inhibitor selectivity. (a) Structural view of divergent residues near the ligand-binding region. APT1 (dark blue) is shown bound to ML348 (green) and APT2 (teal) is shown bound to ML349 (orange). Homologous vertebrate sequences near the β5-α2 loop and G3 helix are shown, highlighting highly divergent (yellow) and less divergent (grey) residues that were selected for mutagenesis. (b) Summary of kinetic and inhibition parameters of APT reciprocal mutants using ResOAc substrate hydrolysis. (c) APT1-I75 and APT2-L78 contribute to inhibitor selectivity caused by isoform-selective steric clashes, highlighted in black dashed lines.

Figure 6. Isoform-selective inhibitors displace sub-micellar fluorescent lipids. (a) APT enzymes enhance BODIPY-FL-C_{16} fluorescence. (b) BODIPY-FL-C_{16} competition with ML348 and ML349 against APT1. (c) BODIPY-FL-C_{16} competition with ML348 and ML349 against APT2.

Table 1: Crystallography Data Collection and Refinement Statistics

Data Collection	APT1·ML348	APT2·ML349
PDB Code	5SYM	5SYN
Space group	*P* 2 2_1 2_1	*C*2
Unit Cell Dimensions		
a, b, c (Å)	71.7, 73.7, 81.8	78.2, 79.8, 138.6
α, β, γ (°)	α=β=γ=90°	α=γ=90°, β=93.3°
Wavelength (Å)	0.9792	0.9786
Resolution (Å)[a]	35.84-1.55 (1.57-1.55)	55.81-1.64 (1.67-1.64)
R_{merge}	0.057 (0.42)	0.095 (0.488)
$I/\sigma(I)$ [b]	18.5 (4.2)	7.1 (2.0)
Completeness (%)[c]	100 (100)	93.2 (84.5)
Redundancy	8.1 (7.8)	3.7(2.9)
Refinement		
Resolution (Å)	1.55	1.64
R_{work}	0.18	0.22
R_{free}	0.20	0.25
Monomers/ASU	2	4
Protein atoms	6909	6615
Heterogen atoms	470	546
Water molecules	362	310
Unique Reflections	63533	97049
r.m.s.deviations		
Bonds (Å)	0.01	0.01
Angles (°)	1.10	1.06
MolProbity Score	1.12	1.08

[a] Statistics for highest resolution bin of reflections in parentheses.

[b] Intensity signal-to-noise ratio.

[c] Completeness of the unique diffraction data.

Figure 1

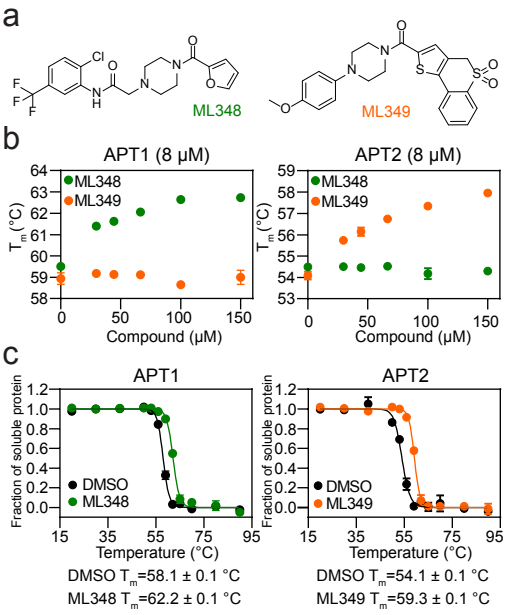
a
ML348
ML349
b
APT1 (8 μM)
APT2 (8 μM)
ML348
ML349
Tm (°C)
Compound (μM)
c
APT1
APT2
Fraction of soluble protein
DMSO
ML348
ML349
Temperature (°C)
DMSO Tm=58.1 ± 0.1 °C
ML348 Tm=62.2 ± 0.1 °C
DMSO Tm=54.1 ± 0.1 °C
ML349 Tm=59.3 ± 0.1 °C

Figure 2

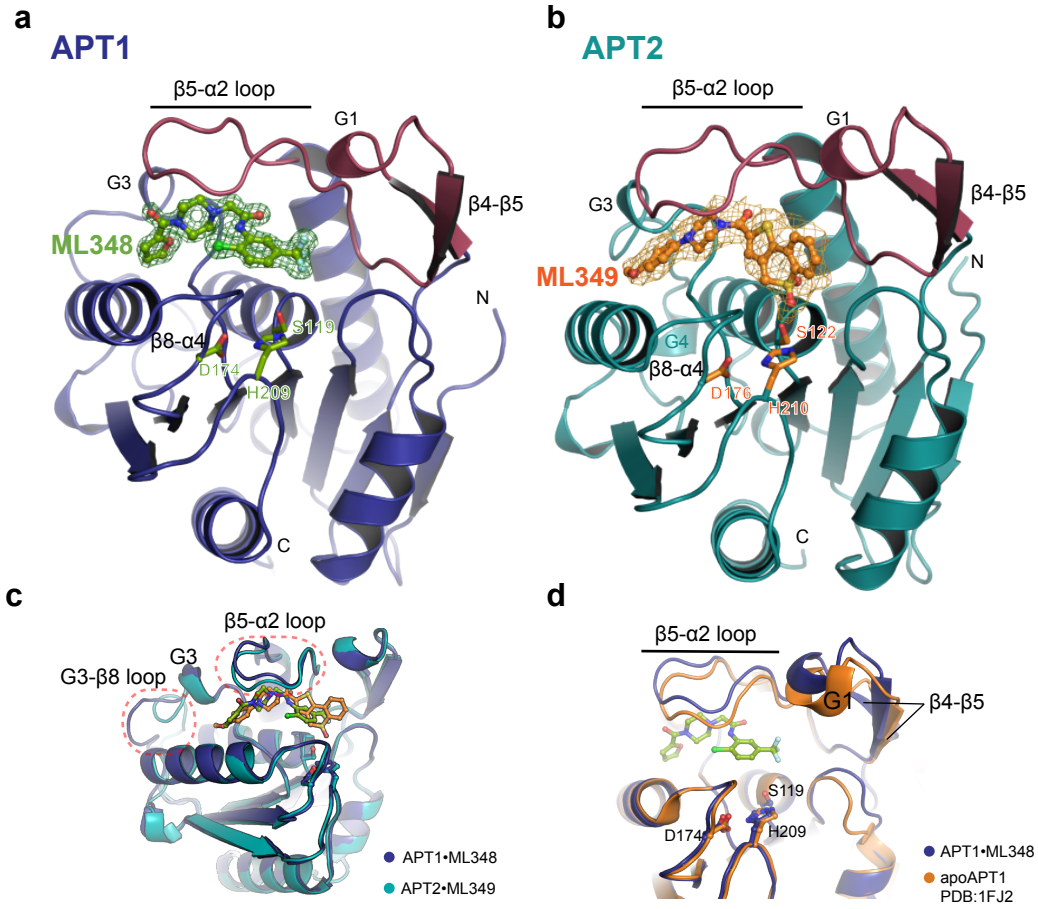
a
APT1
β5-α2 loop
G1
G3
β4-β5
ML348
N
β8-α4
S119
D174
H209
C
b
APT2
β5-α2 loop
G1
G3
β4-β5
ML349
N
G4
β8-α4
S122
D176
H210
C
c
β5-α2 loop
G3
G3-β8 loop
APT1•ML348
APT2•ML349
d
β5-α2 loop
G1
β4-β5
S119
D174
H209
APT1•ML348
apoAPT1
PDB:1FJ2

Figure 3

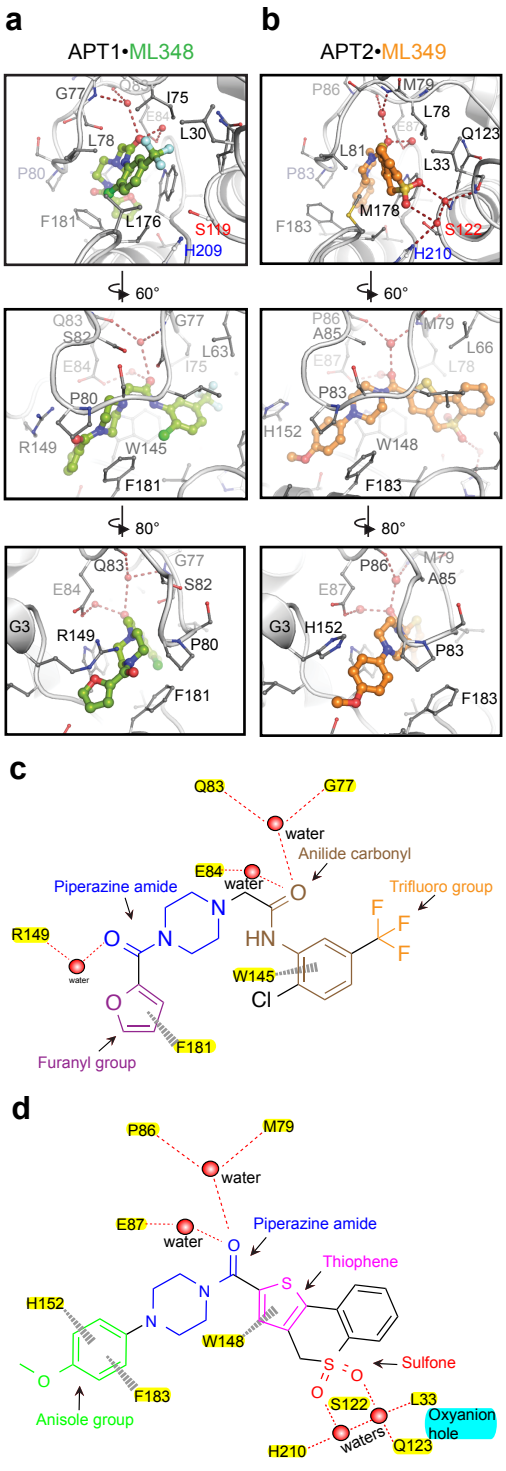
a
APT1•ML348
G77
I75
L30
L78
P80
F181
L176
S119
H209
60°
Q83
S82
G77
L63
E84
I75
P80
R149
W145
F181
80°
Q83
G77
S82
E84
G3
R149
P80
F181
b
APT2•ML349
P86
M79
L78
Q123
L81
L33
P83
M176
F183
S122
H210
60°
P86
A85
M79
L66
E87
L78
P83
H152
W148
F183
80°
M79
P86
A85
E87
G3
H152
P83
F183
c
Q83
G77
water
Anilide carbonyl
E84
water
Piperazine amide
Trifluoro group
R149
water
HN
W145
Cl
Furanyl group
F181
d
P86
M79
water
E87
water
Piperazine amide
Thiophene
H152
W148
Sulfone
F183
Anisole group
S122
L33
Oxyanion hole
H210
waters
Q123

Figure 4

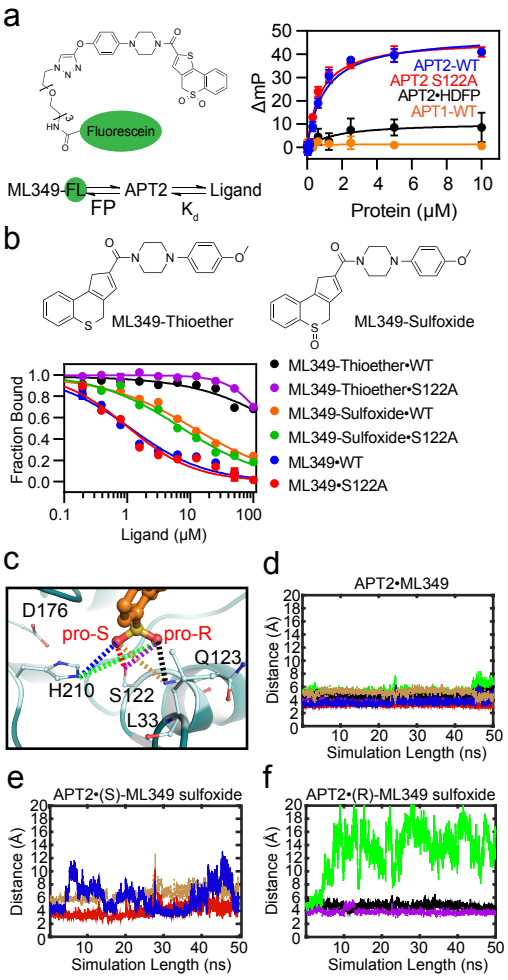
a
Fluorescein
ML349-FL
FP
APT2
Ligand
K_d
ΔmP
APT2-WT
APT2 S122A
APT2•HDFP
APT1-WT
Protein (μM)
b
ML349-Thioether
ML349-Sulfoxide
Fraction Bound
Ligand (μM)
ML349-Thioether•WT
ML349-Thioether•S122A
ML349-Sulfoxide•WT
ML349-Sulfoxide•S122A
ML349•WT
ML349•S122A
c
D176
pro-S
pro-R
Q123
H210
S122
L33
d
APT2•ML349
Distance (Å)
Simulation Length (ns)
e
APT2•(S)-ML349 sulfoxide
Distance (Å)
Simulation Length (ns)
f
APT2•(R)-ML349 sulfoxide
Distance (Å)
Simulation Length (ns)

Figure 5

a

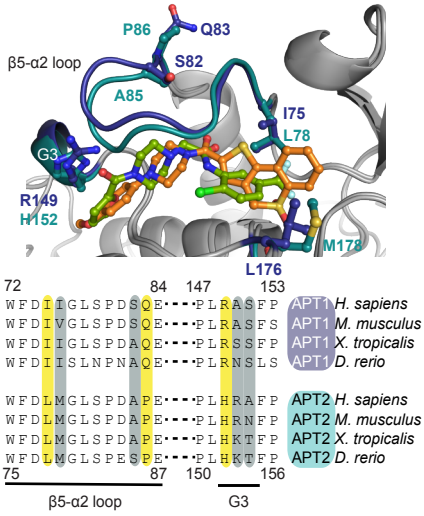

b

	Protein	K_M (μM) ResOAc	K_i (nM) ML348	K_i (nM) ML349
APT1	WT	18 ± 1	280 ± 33	>10000
	L176M	77 ± 1	340 ± 40	>10000
	Q83P	28 ± 1	370 ± 20	>10000
	I75L	23 ± 3	2200 ± 350	370 ± 70
	I75L/S82A	29 ± 1	1200 ± 100	280 ± 20
	I75L/S82A/Q83P	24 ± 1	>10000	1200 ± 70
	I75L/S82A/Q83P R149H/A150R/S151A	25 ± 3	>10000	180 ± 10
APT2	WT	18 ± 2	>10000	120 ± 20
	M178L	19 ± 2	>10000	200 ± 20
	P86Q	32 ± 3	>10000	130 ± 10
	H152R	30 ± 1	>10000	660 ± 50
	L78I	19 ± 1	5800 ± 400	>10000
	L78I/A85S	24 ± 1	6200 ± 310	>10000
	L78I/A85S/P86Q	17 ± 1	3400 ± 260	>10000
	L78I/A85S/P86Q H152R/R153A/A154S	25 ± 1	430 ± 20	>10000

c

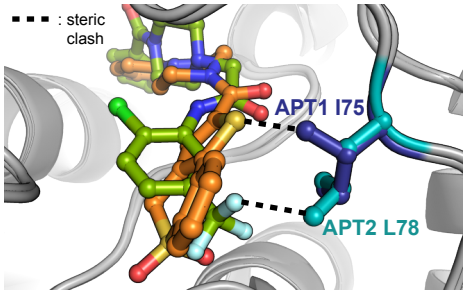

Figure 6

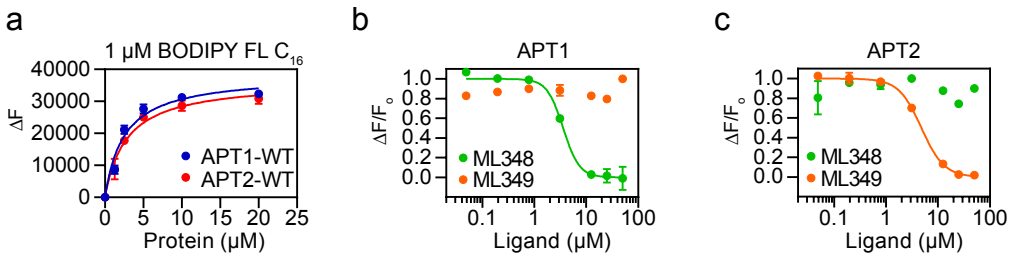
a
1 μM BODIPY FL C16
ΔF
40000
30000
20000
10000
0
0 5 10 15 20 25
Protein (μM)
APT1-WT
APT2-WT
b
APT1
ΔF/Fo
1.0
0.8
0.6
0.4
0.2
0.0
0.1 1 10 100
Ligand (μM)
ML348
ML349
c
APT2
ΔF/Fo
1.0
0.8
0.6
0.4
0.2
0.0
0.1 1 10 100
Ligand (μM)
ML348
ML349